UNIVERSITÄT AUGSBURG
Universitätsbibliothek

OPEN ACCESS
OPUS AUGSBURG

Experimental characterization of the quasi-coherent mode in EDA H-Mode and QCE scenarios at ASDEX Upgrade

J. Kalis, Gregor Birkenmeier, P. Manz, T. Eich, M. Griener, R. Goti, M. Cavedon, L. Gil, M. Faitsch, L. Radovanovic, D. Wendler, E. Wolfrum, U. Stroth

Angaben zur Veröffentlichung / Publication details:

Kalis, J., Gregor Birkenmeier, P. Manz, T. Eich, M. Griener, R. Goti, M. Cavedon, et al. 2024. "Experimental characterization of the quasi-coherent mode in EDA H-Mode and QCE scenarios at ASDEX Upgrade." *Nuclear Fusion* 64 (1): 016038. https://doi.org/10.1088/1741-4326/ad0d32.

Nutzungsbedingungen / Terms of use:

CC BY 4.0

Dieses Dokument wird unter folgenden Bedingungen zur Verfügung gestellt: / This document is made available under these conditions:
CC-BY 4.0: Creative Commons: Namensnennung
Weitere Informationen finden Sie unter: / For more information see:
https://creativecommons.org/licenses/by/4.0/deed.de

nuclear fusion
IAEA

PAPER • OPEN ACCESS

Experimental characterization of the quasi-coherent mode in EDA H-Mode and QCE scenarios at ASDEX Upgrade

To cite this article: J. Kalis *et al* 2024 *Nucl. Fusion* **64** 016038

View the article online for updates and enhancements.

You may also like

- Characterization of the quasi-coherent mode in QCE in experiment and simulation
J Kalis, F Sheffield, G Birkenmeier et al.
- Experimental observation and edge characteristics of EDA H-mode on the HL-3 tokamak
Anshu Liang, Xiaolan Zou, Wulyu Zhong et al.
- ELM-free stationary H-mode plasmas in the ASDEX Upgrade tokamak
W Suttrop, M Maraschek, G D Conway et al.

This content was downloaded from IP address 137.250.100.44 on 09/11/2026 at 13:37

OPEN ACCESS
IOP Publishing | International Atomic Energy Agency
Nuclear Fusion
Nucl. Fusion **64** (2024) 016038 (16pp)
https://doi.org/10.1088/1741-4326/ad0d32

Experimental characterization of the quasi-coherent mode in EDA H-Mode and QCE scenarios at ASDEX Upgrade

J. Kalis[1,2,*], G. Birkenmeier[1,2], P. Manz[3], T. Eich[1], M. Griener[1], R. Goti[1], M. Cavedon[4], L. Gil[5], M. Faitsch[1], L. Radovanovic[6], D. Wendler[1,2], E. Wolfrum[1], U. Stroth[1,2] and the ASDEX Upgrade Team[a] and the EUROfusion MST1 Team[b]

[1] Max Planck Institute for Plasma Physics, Garching, Germany
[2] Physik-Department E28, Technische Universität München, Garching, Germany
[3] Institute of Physics, University of Greifswald, Greifswald, Germany
[4] Dipartimento de Fisica 'G. Occhialini', Università di Milano-Bicocca, Milano, Italy
[5] Instituto de Plasmas e Fusão Nuclear, Instituto Superior Técnico, Universidade de Lisboa, Lisboa, Portugal
[6] Institute of Applied Physics, TU Wien, Fusion@ÖAW, Wiedner Hauptstr. 8-10, 1040 Vienna, Austria

E-mail: Joey.Kalis@ipp.mpg.de

Received 20 April 2023, revised 29 August 2023
Accepted for publication 15 November 2023
Published 8 December 2023



Abstract

The quasi-coherent mode (QCM), appearing in enhanced D_α high confinement mode (EDA H-mode) and quasi-continuous exhaust (QCE) plasmas has been analysed in detail at ASDEX Upgrade via thermal helium beam spectroscopy under various discharge parameters. In both scenarios the QCM appears to be localized close to the separatrix and to propagate in ion diamagnetic direction in the plasma frame. The poloidal wavenumber of the QCM is about $0.025 < k_\theta \rho_s < 0.075$ and the radial wavenumber is $k_r \approx 0\ \mathrm{cm}^{-1}$. It was found that the plasmas are generally below the ideal MHD limit at the separatrix. All the properties are consistent with ideal, resistive or kinetic ballooning modes. Simultaneous to the appearance of the QCM, higher harmonic modes can be observed in EDA H-modes, which are exclusively visible in magnetic pick-up coils and have toroidal mode numbers of up to $n = 10$. By performing a bicoherence analysis it was found that the higher harmonic modes and the QCM are coupling, but are disjoint phenomena. Qualitatively, the bandwidth of the QCM serves as a promising distinctive feature between QCE plasmas and EDA H-modes.

[a] See Stroth *et al* 2022 (https://doi.org/10.1088/1741-4326/ac207f) for the ASDEX Upgrade Team.
[b] See Labit *et al* 2019 (https://doi.org/10.1088/1741-4326/ab2211) for the EUROfusion MST1 Team.
[*] Author to whom any correspondence should be addressed.

Original Content from this work may be used under the terms of the Creative Commons Attribution 4.0 licence. Any further distribution of this work must maintain attribution to the author(s) and the title of the work, journal citation and DOI.

 © 2023 The Author(s). Published by IOP Publishing Ltd on behalf of the IAEA

Keywords: fusion, plasma edge, plasma modes, EDA H-mode, quasi-continuous exhaust, quasi-coherent mode, helium beam diagnostic

(Some figures may appear in colour only in the online journal)

1. Introduction

High-confinement regimes (H-modes) are preferred plasma scenarios for a future fusion reactor [1], but steep pedestal profiles for density and temperature at the plasma edge usually lead to edge-localized modes (ELMs) [2]. The largest type of ELMs, so called type-I ELMs, are a serious concern for ITER [3] and have to be either suppressed [4] or avoided. The latter is achieved by the development of type-I ELM-free operation scenarios [5] like the enhanced D_α high confinement mode (EDA H-mode) or the quasi-continuous exhaust regime (QCE).

The EDA H-mode has been first discovered in Alcator C-mod [6] and was studied in various fusion experiments as DIII-D [7, 8], EAST [9] and ASDEX Upgrade [10]. It features desirable properties for a reactor plasma such as an H-mode-like energy confinement time without type-I ELMs nor signs of impurity accumulation. Furthermore, it is accessibility with pure electron heating and it can be operated near the Greenwald density limit.

The QCE scenario, formerly known as either type-II ELM regime [11] or small ELM regime was also investigated experimentally on TCV [12], JET [13] and ASDEX Upgrade [14–16]. In general, this scenario is accompanied by ELMs with small amplitudes and reduced energy losses compared to type-I ELMs. In ASDEX Upgrade, the QCE and EDA occur in plasmas of similar shape as the in the ITER baseline scenario [17] with the secondary X-point being near the separatrix. But the QCE is situated at higher separatrix densities and higher powers than the EDA H-mode [18].

In both regimes a characteristic edge fluctuation is prominent, called the quasi-coherent mode (QCM), being a known signature of the EDA H-mode [10, 19, 20], and, as shown here, is also linked to the mode shown by Griener *et al* [16] and Wolfrum *et al* [21] in the QCE regime. At Alcator C-Mod, Theiler *et al* [22] has shown, using the gas puff imaging diagnostic that the QCM moves in ion diamagnetic direction with frequency $f \approx 86$ kHz, is localized near the E_r minimum and has a poloidal wavenumber of $k_\theta \approx 1.9$ cm^{-1}. On the other hand, LaBombard *et al* [23] observed the QCM in Ohmic EDA-H discharges with Mirror Langmuir Probes to propagate in electron diamagnetic direction near the scrape-off layer with frequencies around $f \approx 130$ kHz and a poloidal wavenumber of $k_\theta \approx 1.7$ cm^{-1}. Generally, the QCM is believed to be responsible for a strong particle and energy transport at the plasma edge, this way avoiding impurity accumulation and keeping the edge gradients below the peeling-ballooning limit to avoid type-I ELMs. In order to understand and extrapolate a possible EDA H-mode or QCE scenario to large-scale machines like ITER or DEMO [24], it is necessary as a first step to elucidate the properties of the prominent edge fluctuation: the QCM. This paper reports on the properties of the QCM in EDA H-modes and QCE scenarios and outlines similarities and differences of the mode in both regimes using the thermal helium beam (THB) diagnostic [25] and magnetic pick-up coils [26] at ASDEX Upgrade.

Both diagnostics are briefly introduced in section 2 and the experimental results are presented in section 3. First, the appearance of the QCM in frequency space, i.e. the radial localization, the scaling of the frequency of the QCM with different global and local plasma parameters and its bandwidth is examined in section 3.1. Additionally, magnetic pick-up coils measure the QCM as well as higher harmonic fluctuations, hereinafter called HHMs, which turn out to be related. A specific coupling between the QCM and the HHMs is investigated by means of a bicoherence analysis in section 3.2. In section 3.3, the poloidal and radial wavenumber of the QCM is determined and also compared to theoretically motivated wavenumbers. By means of the poloidal wavenumber and the frequency of the QCM, we investigate the velocity of the QCM in the laboratory frame and in the plasma frame in section 3.4. Additionally, all discharges and corresponding data points are characterized in an edge phase space turbulence diagram in section 3.5. By means of all the observed properties of the QCM, a physical interpretation as well as a discussion of the results will be given in section 4. The main results are summarized in section 5.

2. Experimental setup

The experiments were carried out on the ASDEX Upgrade tokamak (AUG) with a major radius of $R_0 = 1.65$ m and minor radius of $a_0 = 0.5$ m. Both EDA H-modes and QCE scenarios are well-established at ASDEX Upgrade (AUG) and can be accessed in a broad range of plasma parameters (cf table 1).

Due to its high temporal (900 kHz) and spatial resolution (3 mm) the THB diagnostic is well suited to investigate the characteristics of the QCM [25]. The basic principle of the THB is the following: the light intensity emitted due to the interaction between plasma electrons and locally injected He atoms is measured at four different He lines for 32 spatial channels or lines of sight (LOS). The measurement of these four spectral He lines allows to deduce information on electron density and temperature by means of a reconstruction algorithm involving collisional radiative modelling (CRM) [27]. He is injected right below the outer midplane by a fast in-vessel piezo valve. The He injection is chopped with a typical puff duration of 50 ms, allowing background subtraction and good radial localization of the light emission. A 2D grid of 5×5 LOS enables 2D intensity measurements in

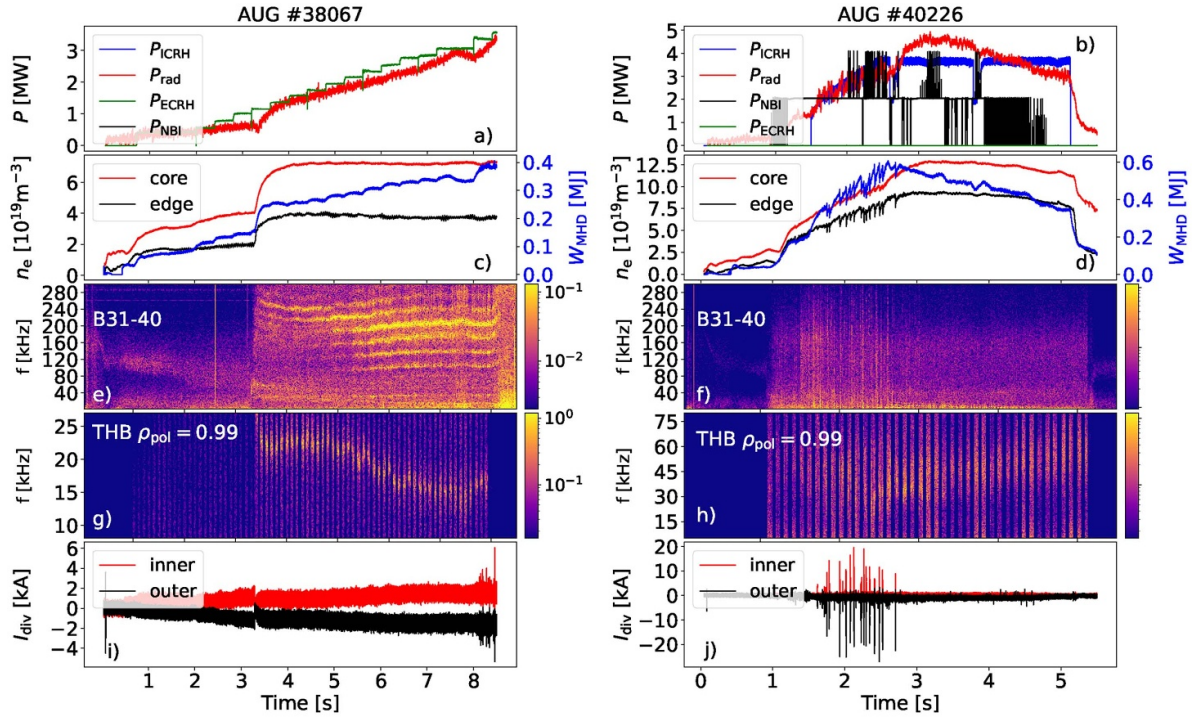

Figure 1. On the left side time traces of the heating and radiated powers (*a*), line averaged electron density and plasma energy content (*c*) and spectrograms from the magnetic pick-up coils (*e*) as well as THB (*g*) are displayed in an EDA H-mode. Additionally, the divertor currents are monitored in (*i*). The corresponding quantities for a QCE discharge are shown on the right side.

the radial-poloidal plane. In general the LOS cover the whole pedestal and extend out into the far scrape-off layer (SOL), as shown in appendix C. In the analysis, it is important to consider diagnostic effects like shadowing or neutral density effects [28, 29], which are avoided by considering not only one individual spectral He line, but the ratio of $\lambda_2 = 667$ nm and $\lambda_1 = 587$ nm [30, 31]. This has been done for all analyses below, i.e. all frequency and wavenumber spectra from THB data were generated from time traces of the ratio of the line intensities at λ_2 and λ_1. The advantage and limitations of considering line ratios instead of absolute (single) intensities is described in [29].

Besides the QCM being visible in the THB, one also observes the QCM and other higher harmonic modes in the magnetic pick-up coils [26] (see figure 5(*a*)), placed at the outer midplane. Magnetic pick-up coils measure deviations from the magnetic equilibrium based on Faraday's law and offer a high temporal resolution, but do not provide radial information.

Time traces of various quantities for one EDA H-mode and QCE discharge are displayed in 1. The graphics on the left side of figure 1 show the EDA H-mode. Here, only Electron Cyclotron Heating (ECRH) is used and after around $t = 3$ s the plasma enters the H-mode, recognizable by the increase in density and plasma energy content. Simultaneously, the magnetic pick-up coil $B31-40$ measures various modes, which will be discussed later, and the THB detects the QCM. Only small activities are observed in the divertor currents, so no type-I ELMs are observed. On the right side, a QCE discharge is shown (the distinction criterion will be introduced in section 3.1). An increase in Ion Cyclotron Heating (ICRH) and Neutral Beam Injection (NBI) carry the plasma in the H-mode like state. No major activity in the magnetic signal is observed, but the QCM is still observed in the THB. In the beginning of the QCE state (between $t = 1.8$ s and $t = 2.6$ s) type-I ELMs, identified as large spikes in the divertor current signal, are observed. After that the ELM activity decreases.

3. Properties of the quasi-coherent mode

To understand the underlying nature of the QCM, we investigate its spectral and spatio-temporal properties as well as their dependence on local plasma quantities. Hence, the QCM is analysed in the following for 13 deuterium plasmas without seeding (for discharges with seeding, see e.g. [32]) at different plasma parameters. This includes variations in toroidal magnetic field strength B_t, plasma current I_P, edge safety factor q_{95} and heating powers P for Electron and Ion Cyclotron Heating (ECRH, ICRH) and Neutral Beam Injection (NBI). The range of plasma parameters is listed in table 1. It has to be mentioned that six discharges are classified as EDA H-modes and seven as QCE scenarios, according to the distinction criterion in section 3.1.

In the following all profile quantities like the local electron density n_e, temperature T_e, pressure p_e and the electron pressure gradient ∇p_e are taken from integrated data analysis (IDA) [33], if not stated otherwise.

Table 1. Discharge parameters of EDA and QCE plasmas covered by the analysed data set.

Type	B_t (T)	I_P (MA)	q_{95}	P_{ECRH} (MW)	P_{ICRH} (MW)	P_{NBI} (MW)
EDA	2.50	0.60–0.79	5.32–6.64	1.9–3.5	0.0	0.0–2.5
QCE	1.90–2.52	0.71–1.10	3.69–5.61	0.0–4.4	0.0–3.9	0.0–5.0

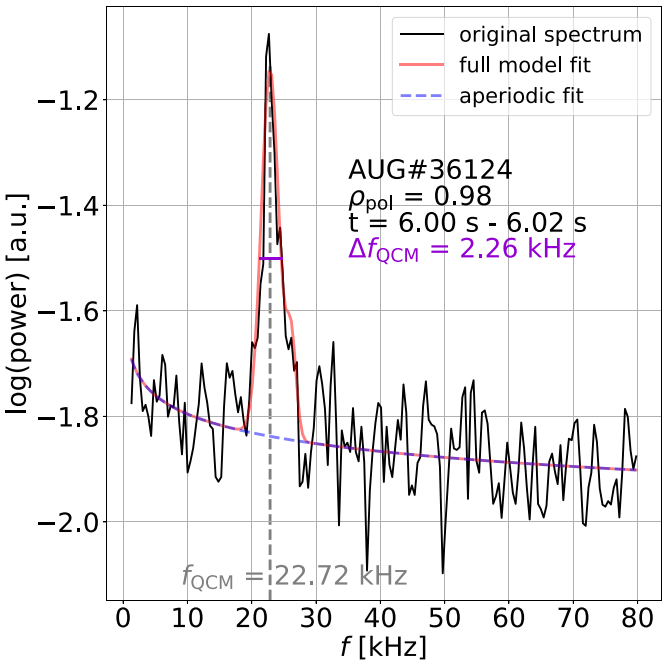

Figure 2. Example of a THB line ratio Fourier spectrum for an EDA H-mode #36124. The QCM is found at $f_{QCM} = 22.72$ kHz and fitted (red) by a model, adapted from [34].

3.1. Appearance in frequency space

The temporal QCM properties of interest are the frequency, the coherency, the amplitude and the scaling of the frequency with given plasma parameters. These properties and the coupling of the QCM with other modes (section 3.2) are described in the following and can later be used to distinguish between EDA H-modes and QCE plasmas.

Figure 2 shows the Fourier spectrum of the time trace of the line ratio λ_2/λ_1 of the THB taken at $\rho_{pol} = 0.98$ for discharge #36124, averaged over a time interval of $\Delta t = 20$ ms. ρ_{pol} is defined as

$$\rho_{pol} = \sqrt{\frac{\Psi - \Psi_a}{\Psi_{sep} - \Psi_a}}, \tag{1}$$

where Ψ is the magnetic flux and Ψ_a the corresponding magnetic flux at the magnetic axis and Ψ_{sep} at the separatrix. Three details of the QCM are obtained from this type of frequency spectrum: the frequency of the mode f_{QCM}, the height of the spectral peak at the QCM frequency, and the width of the peak, i.e. the bandwidth of the QCM Δf_{QCM}.

By comparing the Fourier spectra along the radial extent of the THB LOS, we localize the mode ρ_{pol}^{QCM} where the highest relative peak in the Fourier spectrum of the line ratio time trace (λ_2/λ_1) occurs. The relation of the measured quantity and the corresponding density and temperature fluctuations is verified in appendix B via a simulation of a synthetic localized mode, evaluating its appearance in raw intensities. For this purpose, the background (aperiodic fit) was subtracted from the original spectrum, so that a Gaussian-like function is fitted to the residual data (more details in [34]). The QCM is found to be localized close to the separatrix at the normalized plasma radius of $\rho_{pol}^{QCM} = 0.993 \pm 0.007$ in all discharges. This matches a distance of $\Delta R \approx 7$ mm inside the separatrix. The results for individual discharges are shown in table A1. Figure 11(*b*) (purple line) shows an example of the QCM amplitude profile and its maximum determined by this method. In the following, all plasma quantities and QCM properties are determined at the radial position, at which the mode is localized by this method.

Next it is studied how the QCM frequency depends on local plasma parameters. Since the mode is located at the edge, where strong $E \times B$ flows are present, a natural frequency dependence might occur due to the fact that the QCM is connected with the local plasma velocity $v_{E\times B}$. According to this, f_{QCM} should be higher in plasmas with higher $E \times B$ flows at the plasma edge. Figures 3(*a*) and (*b*) show that the temporal evolution of f_{QCM} does not follow the trend of the approximated plasma velocity $v_{E\times B} = E_r/B_t \approx \nabla p_e/(B_t e n_e) = v_{e,dia}$, which is manifested in figure 3(*e*) for many discharges. Here, E_r is the radial electric field, ∇p_e is the electron pressure gradient, e is the elementary charge and n_e is the local electron density. To set $v_{E\times B} \approx v_{e,dia}$ is motivated by the observation at AUG in [35] that E_r is close to its neoclassical value at its minimum. In section 3.4, it will be shown with data of direct measurements of E_r by means of Charge Exchange Recombination Spectroscopy (CXRS) [36] that this assumption slightly inside the separatrix is reasonable.

If the QCM would be of Alfvénic nature, a frequency dependence of $v_A \sim B/\sqrt{n_e}$ is expected, where B can be either the toroidal (B_t) or the poloidal (B_{pol}) magnetic field strength. The latter case was found for the M-mode at JET [37]. In figure 3(*f*) the poloidal Alfvén velocity is written as $v_{A,\theta} \propto I_p/\sqrt{n_e}$. The comparison shows that the experimental results disagree with this scaling, i.e. f_{QCM} does neither scale with $B_{pol}/\sqrt{n_e}$ nor with $B_t/\sqrt{n_e}$ (not shown here).

For type-III ELMs, it has been speculated that the frequency is increasing with resistivity η (figure 3(*c*)) [2]. Figure 3(*g*) finds such a scaling for isolated cases, but a general proportionality for all discharges is not suggested by the data.

As a best fit, a heuristic dimensionless relation for f_{QCM} was found as (figure 3(*h*))

$$\frac{f_{QCM}}{c_s/R_0} = \frac{1}{(2\pi)^2 q^2 \beta_e^2} = \frac{R_0^2}{(2\pi a_0)^2 \beta_{pol}^2}, \tag{2}$$

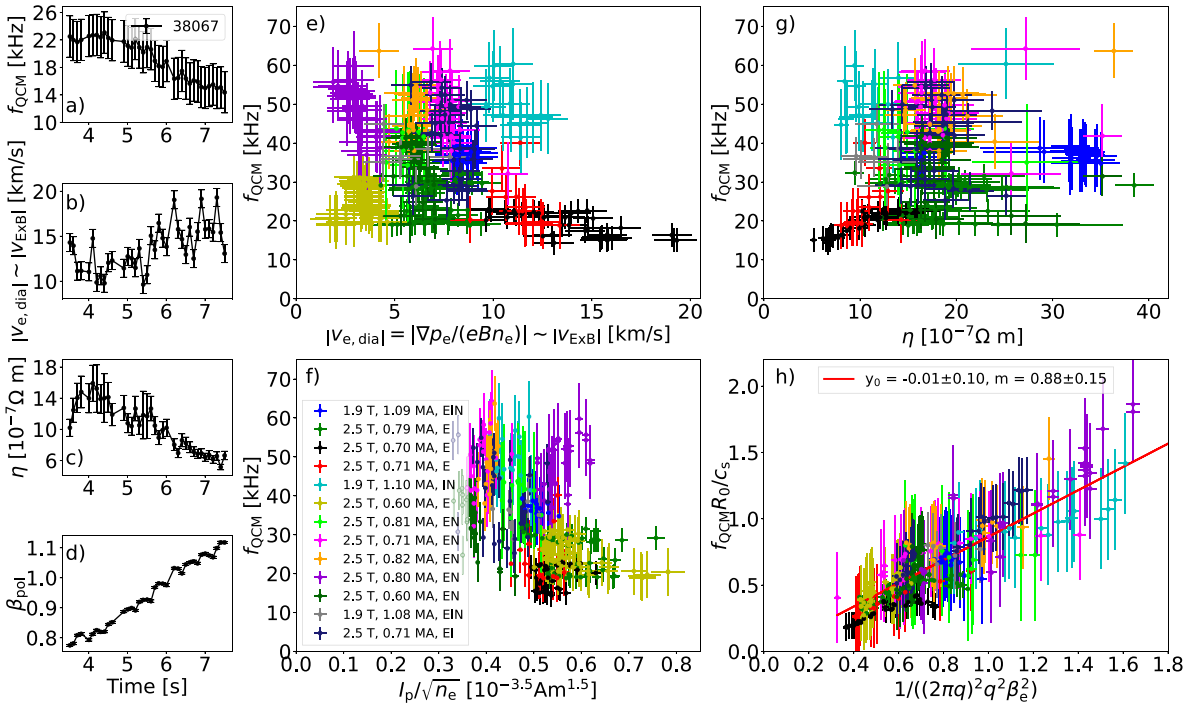

Figure 3. Temporal behaviour of f_{QCM}: (*a*) the approximated plasma velocity $v_{E\times B}$ (*b*), resistivity η (*c*) and the poloidal plasma parameter β_{pol} (*d*) for EDA H-mode discharge #38067. For various discharges, f_{QCM} or $f_{QCM}R_0/c_s$ is drawn against (*e*) $v_{E\times B}$, (*f*) the poloidal Alfvén velocity approximated by $I_p/\sqrt{n_e}$, (*g*) resistivity η and (*h*) $1/\beta_{pol}^2$. y_0 (offset) and m (slope) in (*h*) are the corresponding parameters for a linear fit. The legend includes the toroidal field strength B_t, plasma current I_P and the used heating method, where E: ECRH, I: ICRH, N: NBI.

where $c_s \sim \sqrt{T_e/m_i}$ is the ion sound speed, $\beta_{pol} = \mu_0 n_e T_e/B_{pol}^2$ is the poloidal plasma beta, and $\beta_e = \mu_0 n_e T_e/B_t^2$. The errors of the linear fit are calculated as the standard deviation of the maximum and the minimum possible slope, including the errors of the experimental data. Equation (2) is similar to the results of Birkenmeier *et al* [38] ($f_{LCO} \sim 1/\beta_e$) and Grover [39] ($f_{LCO} \sim 1/\sqrt{\beta_e}$) for Limit Cycle Oscillations (LCO) in I-phase plasmas. The latter model bases on a predator-prey-like coupling between the in-out asymmetry in the pressure and an up-down asymmetric flow perturbation, i.e. the Stringer spin up mechanism [40] might play a major role (see [39]).

Lastly, the bandwidth of the QCM, Δf_{QCM}, is analysed, exemplary for discharge #40110, in which ECRH is replaced gradually by ICRH (figure 4(*a*)). Δf_{QCM} is calculated from the corresponding Fourier spectrum as the FWHM of the Gaussian-like peak in figure 2. This procedure has been performed for different time intervals to gain a time evolution of Δf_{QCM}. The spectrogram in figure 4(*b*), evaluated at $\rho_{pol} = 0.996$, indicates that the QCM gets fainter and broader in frequency space when plasma heating is changed from ECRH to ICRH. Figure 4(*c*) indicates that a higher QCM frequency leads to a larger bandwidth qualitatively.

Now we address signatures of the QCM [41] or of other modes in the magnetic pick-up coils by means of the magnetic spectrogram for coil $B31-40$ in figure 4(*d*). The coil is located at the outer midplane measuring the radial magnetic field component. We note that other modes, hereinafter referred to as higher harmonic modes (HHMs), can accompany the QCM. Both kinds of modes are highlighted in the Fourier spectrum of the magnetic coil in figure 5. The QCM with $f_{QCM} = 22.7$ kHz is very close to the lowest frequency HHM with $f_{HHM,n=1} \approx 30$ kHz and toroidal mode number of $n = 1$. n was determined by means of the toroidal mode determination method as described in [42]. In figure 4(*d*) it is visible that the HHMs vary during the discharge. At the beginning, HHMs are clearly visible as equidistant horizontal stripes, i.e. higher harmonics of a base frequency with $f_{HHM} \approx \ell \cdot 30$ kHz with $\ell = 4, \ldots, 8$. Then (between $t_0 = 3.3$ s and $t_1 = 5.1$ s) the HHMs get less visible, but also ELMs appear in the divertor current in figure 4(*e*), influencing the magnetic signal. Between $t_1 = 5.1$ s and $t_2 = 7.5$ s the HHMs seem to get broader so that they cannot be distinguished from each other and in the end, they are not observable anymore. Thus, it seems natural to consider a correlation between the presence of the HHMs and the coherency of the QCM quantified as $\Delta f_{QCM}/f_{QCM}$.

We define a measure of the visibility of the HHMs as

$$\log V_{HHM} = \log(HN), \tag{3}$$

where H is the peak height of the most dominant mode in the magnetics, and N is the number of HHMs present in the signal. The higher $\log V_{HHM}$, the better is the visibility of HHMs in the signal. An example of the quantities influencing $\log V_{HHM}$ is presented in figures 5(*a*) and (*b*). For figure 5(*a*) the amplitude amounts to $H = 1.17$ and we find $N = 8$, resulting in $\log V_{HHM} = 0.97$.

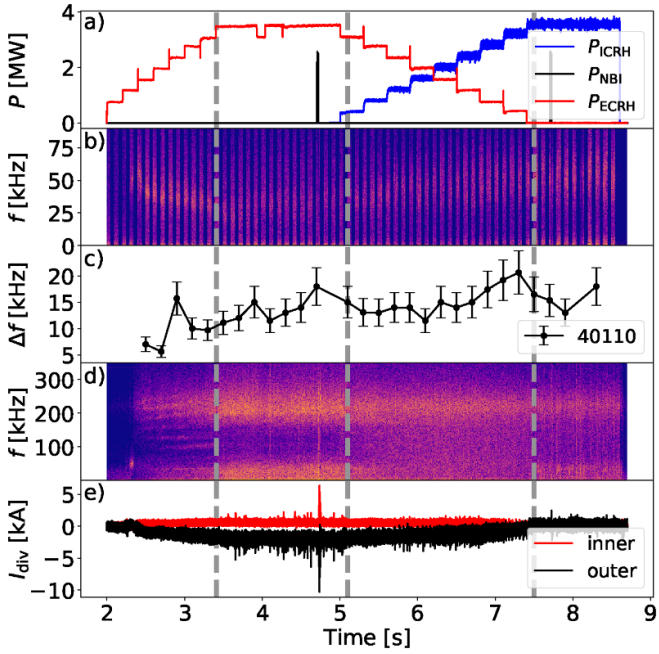

Figure 4. Temporal evolution of heating power of different mechanisms for AUG discharge #40110 (*a*). The QCM bandwidth Δf (*c*) increases qualitatively during the discharge. The vertical stripes in the spectrogram of the THB data (*b*) are due to the THB chopping every 50 ms. In the spectrogram, obtained by the magnetics (*d*), the HHMs are also changing in the different intervals (grey dotted lines). (*e*) Shows the divertor current to monitor the ELM activity.

Figure 6 compares this quantity with spectral properties of the QCM for the same set of discharges as introduced above. Although a trend between the coherency (6(*a*)) or the bandwidth (6(*b*)) and $\log V_{\mathrm{HHM}}$ is noticeable, the most appropriate is obtained between f_{QCM} and the presence of HHMs (6(*c*)). Hence, a QCM with low frequency is able to coexist with the HHMs.

Additionally, a general relationship between the applied heating mechanism and the spectral behaviour of the QCM is not obtained, but the most coherent QCMs are achieved in ECRH-only plasmas (figure 6(*b*)).

As described in section 1 and shown in figure 1, QCE discharges are usually accompanied by ELMs or filaments with small amplitudes and EDA-H discharges do not feature ELMs. These ELMs may transfer heat and particles into the SOL and vary n_{e} and T_{e} and hence β_{e} at the plasma edge strongly. A variation in β_{e} leads to a variation of f_{QCM}, according to equation (2). This is displayed in an increase in Δf_{QCM} for QCE discharges. Therefore, the bandwidth of the QCM is used to distinguish EDA H-modes from QCE discharges. In the following analyses, an arbitrary boundary of

$$\Delta f_{\mathrm{QCM}} = 10\ \mathrm{kHz} \tag{4}$$

is introduced, so that discharge phases, in which a coherent mode appears, i.e. with $\Delta f_{\mathrm{QCM}} < 10$ kHz are defined as EDA-H modes and discharge phases with $\Delta f_{\mathrm{QCM}} > 10$ kHz as QCE regime. This boundary is chosen, because it yields two subsets of data points in figures 6(*a*) and (*b*) and consequently, these subsets lead to different behaviour patterns in the separatrix $\alpha_{\mathrm{d}} - \alpha_{\mathrm{MHD}}$−diagram, discussed in section 3.5.

3.2. Coupling of QCM and magnetic modes

Both, the QCM and the HHMs are observed in the magnetic pick-up coils (see e.g. figures 5 and 7(*a*)). As shown in figure 6(*c*), the modes seem to be connected since a higher visibility of HHM correlates with a lower frequency of the QCM. Generally, the most prominent HHMs have toroidal mode numbers n in the range of $n = 5$ to $n = 8$ with frequencies of $f_{\mathrm{HHM}} = 150$ kHz to 240 kHz, whereas the fundamental mode ($n = 1$) has a frequency of $f_{\mathrm{n=1}} \approx 30$ kHz, which is close to the QCM frequency but usually higher than it.

It appears likely to examine whether and to what extent the QCM shows a causal relationship to the HHMs or if their simultaneous occurrence is not correlated. Another natural condition for a causality between those modes is that their phase difference must be rigid, enabling a coupling. The coupling can be analysed with a bicoherence analysis [43]. Figure 7(*b*) shows an auto-bispectrum of the magnetic signal from coil $B31 - 40$, implying that the HHMs couple to each other and to the QCM. Here, the data was averaged over 10 ms. Two points in the bispectrum show the interaction between the HHMs and the QCM (see enlarged window): one right below the abscissa ($f_1 = 200$ kHz, $f_2 = -18$ kHz) and one close to the diagonal for $f_2 < 0$ kHz ($f_1 = 200$ kHz, $f_2 = -182$ kHz). To further investigate the QCM-HHM coupling, a bicoherence analysis was performed for every 40 ms. Figure 7(*c*) shows the comparison of the frequency coordinates close to the diagonal (latter case) from the bicoherence analysis and the frequencies of the modes in the magnetic spectrogram from figure 7(*a*). The bicoherence frequencies f_1 and f_2 are marked as blue and white data points. We see that f_1 agrees with the frequency of the most prominent HHM, but f_2 is not visible, or only faintly. Contrary, their sum frequency $f = f_1 + f_2$ is equal to the frequency of the QCM. Hence, the QCM and the most prominent HHM are coupling. This can be interpreted in two ways: either the QCM at $f_{\mathrm{QCM}} = 18$ kHz and the most prominent HHM at $f_{\mathrm{HHM,n=6}} = 200$ kHz couple together producing a third mode at 182 kHz, or the unknown weakly visible mode at 182 kHz and the strongest HHM at $f_{\mathrm{HHM,n=6}}$ couple together producing the QCM. However, the QCM is certainly not a result of the HHMs, because the mutual coupling of the interaction of different harmonics of the HHMs yield always a mode with a frequency of a multiple of the fundamental $n = 1$ mode. In other words: if you pick a combination of f_1 and f_2 other than the ones proposed before in figure 7(*b*), their sum frequency is equal to $\ell \cdot f_{\mathrm{n=1}}$, where $\ell \in \mathbb{N}$.

The fact that the HHMs do not cause the QCM is also underlined by the different time evolution of their frequencies, i.e. when f_{HHM} increases with time f_{QCM} generally decreases.

Furthermore, in many QCE scenarios we observed the QCM but no HHMs or other high frequency modes, affirming the fact that the QCM can exist an absence of the HHMs or any other type of mode visible in the magnetics. This indicates

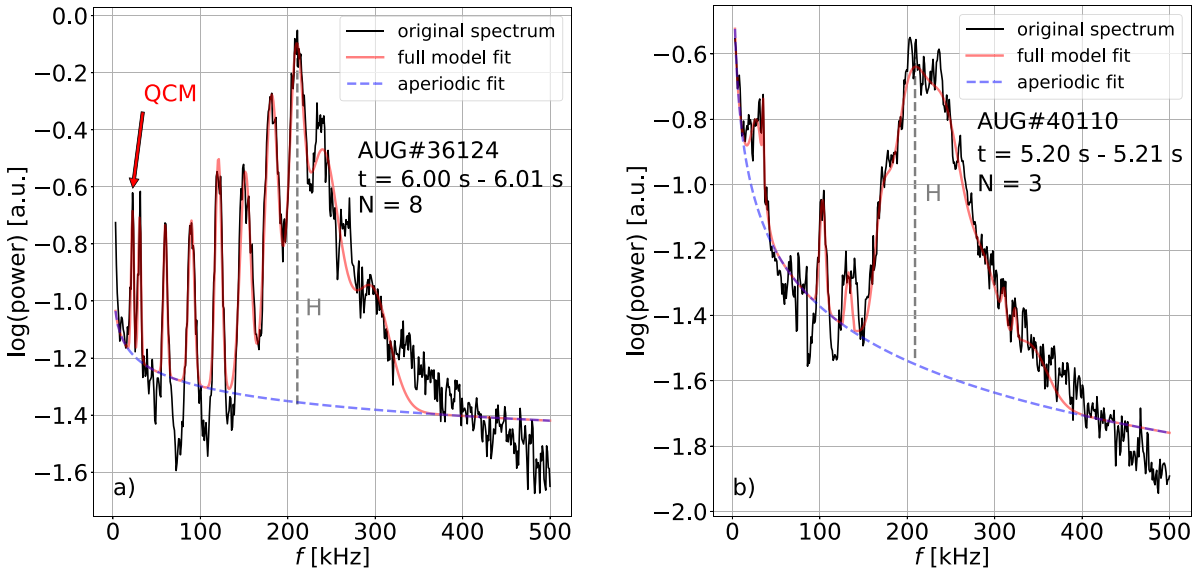

Figure 5. Example of a Fourier spectrum for an EDA H-mode #36124 (*a*) and QCE time points of discharge #40110 (*b*) in the magnetic pick-up coil $B31-40$, in which the QCM and the HHMs are visible. The fitting model is adapted from [34].

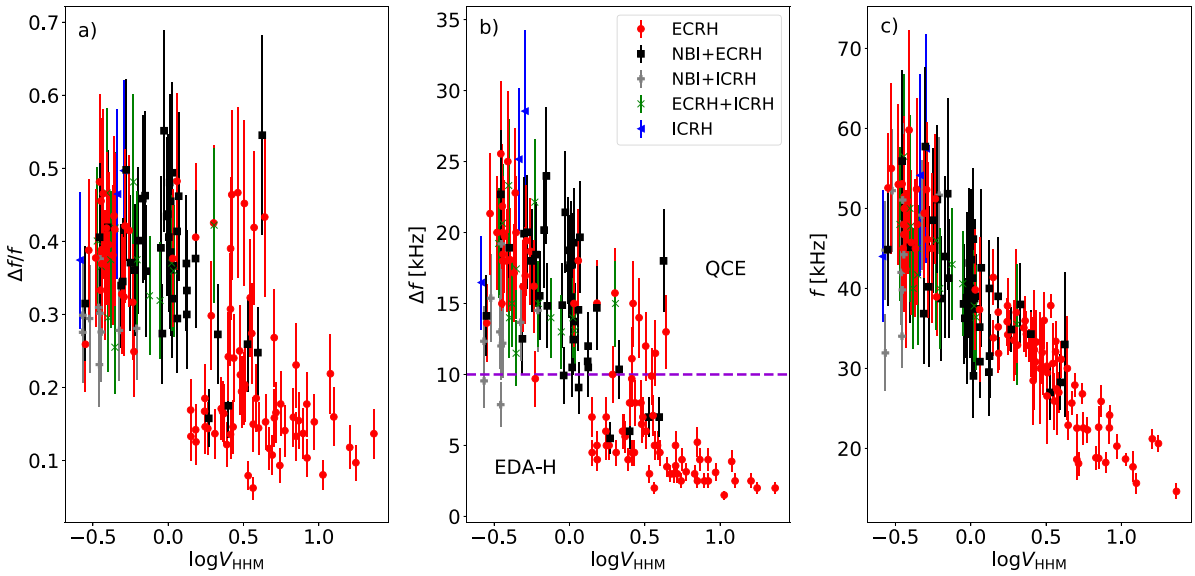

Figure 6. Correlation between the visibility of the HHMs $\log V_{\mathrm{HHM}}$ and the coherency $\Delta f_{\mathrm{QCM}}/f_{\mathrm{QCM}}$ (*a*), the bandwidth Δf_{QCM} (*b*) and the frequency f_{QCM} (*c*) for different heating mechanisms applied. An arbitrary boundary to distinguish EDA H-modes from QCE scenario is set to $\Delta f_{\mathrm{QCM}} = 10$ kHz, indicated by the purple horizontal line.

that the QCM is an independent mode driven by a separate mechanism.

3.3. Poloidal and radial wavenumber of the QCM

After analysing the coupling of the QCM with the HHMs based on magnetic signals, we now return to the determination of properties of the QCM by means of the THB. In contrast to the frequency, which depends on the plasma background velocity, the wavenumber is not affected by this and represents therefore a robust mode property directly accessible by local measurements in the laboratory frame. The poloidal wavenumber k_θ represents the poloidal size of the QCM as $\lambda_\theta = 2\pi/k_\theta$. It is calculated by the method introduced by Beall *et al* [44], for which it is necessary to determine the cross-correlation of two THB line ratio time series acquired at two poloidally aligned channels and divide their phase difference by the distance Δ of the respective channels (see the grid arrangement in appendix C).

Figure 8(*a*) shows a typical $k_\theta - f$ spectrum for one time interval of 40 ms, which is of the order of an active He puffing phase for discharge #38067, in which a heating power ramp-up was implemented. The colour scale indicates whether there is a mode with a specific combination of k_θ and f. In this example, the mode activity concentrates around $k_\theta = -0.64\mathrm{cm}^{-1}$ and $f \approx 17.1$ kHz. The found frequency is equal

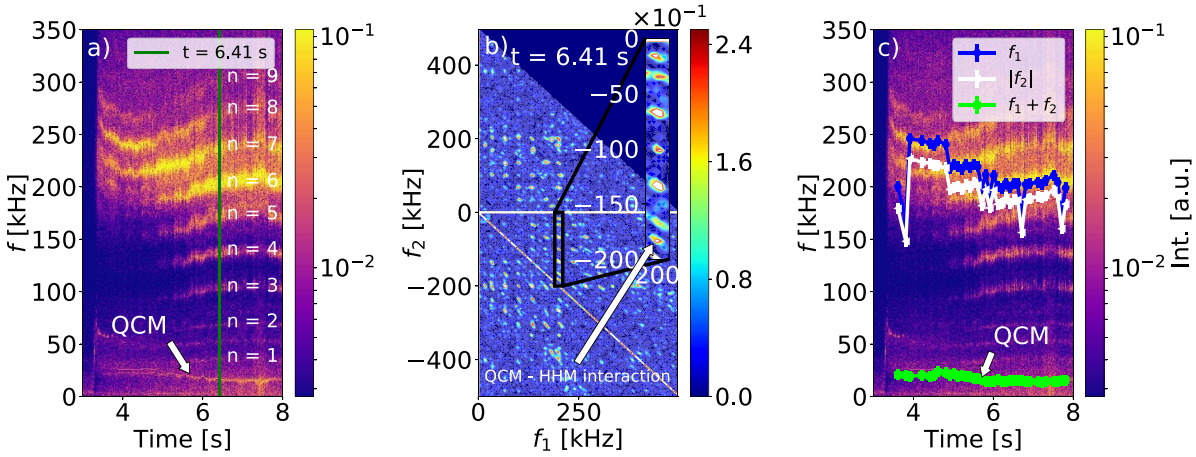

Figure 7. (*a*) Spectrogram of one magnetic pick-up coil in discharge #38067 with QCM and HHM signature. HHMs are assigned with toroidal wavenumbers of up to $n = 9$. The green line $t = 6.41$ s indicates at which a bicoherence analysis is performed in (*b*). The temporal evolution of the combinations for (f_1, f_2) as marked in the enlarged section and their sum, $f_{\mathrm{QCM}} = f_1 + f_2$ are shown in (*c*).

to the one of the QCM as determined in the standard Fourier spectrum, yielding the corresponding poloidal wavenumber of the QCM of about $k_\theta^{\mathrm{QCM}} = -0.64\ \mathrm{cm}^{-1}$. The negative sign of k_θ indicates that the mode propagates in electron diamagnetic direction in the laboratory frame, but in the following only the absolute value of k_θ is used. By evaluating the $k_\theta - f$ spectra for small and consecutive time intervals of 20 ms, it is possible to analyse the temporal evolution of k_θ and the influence of local or global plasma parameters on k_θ during the whole discharge. Figure 8(*b*) presents the time series of k_θ at a radial position right inside the separatrix at $\rho_{\mathrm{pol}} = 0.995$. The error bars σ_{k_θ} correspond to the FWHM along the k_θ-axis from the $k_\theta - f$ spectrum at the frequency of maximum amplitude (the QCM frequency). Furthermore, we compare k_θ for different discharges and thus, different plasma parameters. k_θ and f are connected via the phase velocity in the laboratory frame as $v_{\mathrm{lab}} = 2\pi f/k_\theta$, which will be discussed in section 3.4. The values of k_θ deviate for ASDEX Upgrade [10] and Alcator C-Mod [22, 23]. In order to make comparisons to other tokamaks and to theoretical approaches, the poloidal wavenumber normalized to the hybrid gyroradius $k_\theta \rho_{\mathrm{s}}$ is used, where $\rho_{\mathrm{s}} = \sqrt{T_{\mathrm{e}} m_{\mathrm{i}}}/eB$. This is depicted in figure 8(*c*). k_θ varies by less than a factor of two in this discharge, $k_\theta \rho_{\mathrm{s}}$ changes from 0.038 to 0.075. The reason for this difference is the change of the electron temperature T_{e}, which enters the definition of ρ_{s}. n_{e} is nearly constant during the discharge and a comparison between k_θ, $k_\theta \rho_{\mathrm{s}}$ and the profile quantities T_{e} and p_{e} shown in figures 8(*d*)–(*f*), respectively, leads to the observation that a scaling law between those exists, which will be shown quantitatively in the following.

After a promising relation for the frequency of the QCM f_{QCM} has been found (see equation (2) above), we now try to find a correlation of $k_\theta \rho_{\mathrm{s}}$ with plasma parameters guided by theoretical considerations. The Drift-Alfvén (DALF) model [45] is a system of plasma fluid equations and describes turbulence at the plasma edge in toroidal geometry. Based on the DALF model it is possible, to differentiate between three regimes: the electromagnetic (EM), the resistive ballooning mode (RBM) and the ideal ballooning mode (IBM) regime. This discrimination was proposed in a similar way by Rogers *et al* [46]. All three regimes are characterized by a specific scaling of the poloidal mode number, which are derived in [47]:

$$k_{\mathrm{EM}} \rho_{\mathrm{s}} = \sqrt{\frac{\mu_0 m_{\mathrm{i}} p_{\mathrm{e}}}{B_{\mathrm{t}}^2 m_{\mathrm{e}}}}, \tag{5}$$

$$k_{\mathrm{RBM}} \rho_{\mathrm{s}} = K \frac{\sqrt{\alpha_{\mathrm{c}}} T_{\mathrm{e}} \lambda_{\mathrm{p_e}}^{1/4}}{q_{95}^2 \sqrt{n_{\mathrm{e}}}}, \tag{6}$$

$$k_{\mathrm{ideal}} \rho_{\mathrm{s}} = C \frac{T_{\mathrm{e}}^{3/2}}{\lambda_{\mathrm{p_e}}^{1/4} B_{\mathrm{t}}}. \tag{7}$$

μ_0 is the magnetic permeability, m_{e} is the electron mass, $\alpha_{\mathrm{c}} = \kappa_{\mathrm{geo}}^{1.2}(1 + 1.5\delta)$ is the critical α_{MHD} (section 3.5) with the geometrical parameters elongation κ_{geo} and triangularity δ, $\lambda_{\mathrm{p_e}} = p_{\mathrm{e}}/\nabla p_{\mathrm{e}}$ is the typical perpendicular gradient length, and $K = 792 \times 10^6\ \mathrm{eV}^{-1}\mathrm{m}^{-7/4}$ and $C = 688 \times 10^{-6}\ \mathrm{m}^{1/4}\mathrm{eV}^{-3/2}\mathrm{T}$ are the corresponding constants for AUG.

k_{EM} describes the transition between the electromagnetic ($k_\theta < k_{\mathrm{EM}}$) and the electrostatic regime ($k_\theta > k_{\mathrm{EM}}$) in wavenumber space at low collisionality. k_{RBM} is the typical wavenumber of the electrostatic RBM and k_{ideal} describes the transition between the ideal ($k_\theta < k_{\mathrm{ideal}}$) and resistive MHD-like ($k_\theta > k_{\mathrm{ideal}}$) regime in wavenumber space. These are typical wavenumbers, for which one does not expect an exact match with the maximum growth rates. However, these are well-defined quantities whose scaling can be well studied analytically and in numerical investigations. If a scaling with the quantities is found experimentally, this would be helpful for further theoretical investigations.

In figure 9, the experimental values of $k_\theta \rho_{\mathrm{s}}$ are compared to all three quantities. The electromagnetic wavenumber $k_{\mathrm{EM}} \rho_{\mathrm{s}}$ reproduces the experimental trend the best. An increase in $\sqrt{\beta}$ leads to a higher wavenumber. That the experimental values

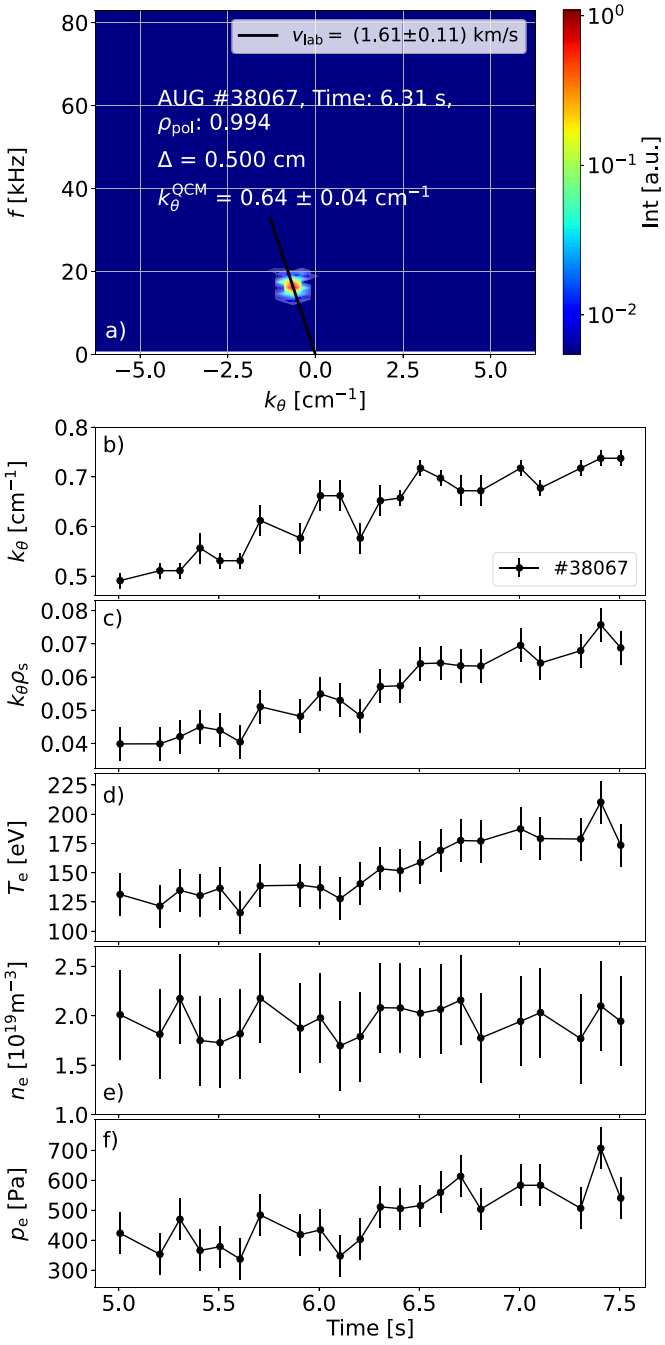

Figure 8. Example of a $k_\theta - f$ spectrum in discharge #38067 for the time interval $t = [6.30\text{ s}, 6.34\text{ s}]$ (*a*), where the spot of high intensity marks the QCM. The slope of the black line displays the phase velocity in the laboratory frame v_{lab}, but it is calculated just at the high intensity point for the corresponding values of k_θ and the frequency. k_θ (*b*) and the normalized wavenumber $k_\theta\rho_s$ (*c*) vary during the discharge. Local electron temperature (*d*), density (*e*) and pressure (*f*) are measured at $\rho_{pol} \approx 0.995$ for the same discharge.

scale well with $k_{EM}\rho_s$ is further supported by a small offset (y_0), indicating that the poloidal wavenumber depends on the normalized energy content of the plasma. In the case of the characteristic RBM wavenumber $k_{RBM}\rho_s$ in figure 9(*b*) and the IBM wavenumber $k_{ideal}\rho_s$ in figure 9(*c*), the offset of the linear fit is larger and the data points are more scattered. In all cases, the absolute values are not reproduced since the slope is $m \ll 1$, which has been explained above.

Overall, the measured values of the poloidal wavenumber of $0.025 < k_\theta\rho_s < 0.075$ are in a range between micro-instabilities ($k_\theta\rho_s > 0.1$) and typical MHD modes ($k_\theta\rho_s < 0.01$), and in a range, where EM effects are expected to become important.

In figure 10(*a*) the radial structure of the mode and the radial wavenumber k_r is determined by cross-correlating radially aligned THB LOS. As shown in figure 10(*b*), the radial wavenumber is approximately zero for a radial region between $\rho_{pol} = 0.994$ and $\rho_{pol} = 1.002$. In addition, the measured laboratory velocity of $v_{lab} \gg 1\text{ km s}^{-1}$ might indicate the occurrence of streamers [48]. Streamers are radially elongated flows, transporting heat and particles into the far SOL. Additionally, figure 10(*b*) shows that $k_r > 0\text{ cm}^{-1}$ inside the pedestal and that it shrinks to a small value at the position of the QCM close to the separatrix. $k_r > 0\text{ cm}^{-1}$ means that the QCM signal was first measured further in and then further out, indicating a radial movement towards the highest QCM amplitude, i.e. radial outwards.

3.4. Phase velocity of the QCM

The phase velocity in the co-moving plasma frame v_{pl}, is an important quantity of a mode due to the fact that the direction of motion excludes potential underlying instabilities. v_{pl} is given as the difference of the mode velocity in the laboratory frame v_{lab}, obtained from the $k_\theta - f$ spectrum (cf figure 8(*a*)), and the $E \times B$ background plasma velocity,

$$v_{E\times B} \approx E_r/B_t = \left(\frac{1}{n_i Z_i e}\nabla p_i - v_{pol,i}B_t + v_{t,i}B_{pol}\right)/B_t, \quad (8)$$

i.e. $v_{pl} = v_{lab} - v_{E\times B}$. Z_i is the effective main ion charge number in the plasma, $v_{pol,i}$ is the poloidal and $v_{t,i}$ the toroidal rotation velocity. This expression requires the measurement of ion data, like the ion pressure p_i. On AUG $v_{E\times B}$ is routinely measured by edge CXRS [36]. This implies that NBI heating is a necessity to determine $v_{E\times B}$ by means of CXRS. Though, on AUG $v_{E\times B}$ is close to the negative ion diamagnetic velocity $v_{i,dia}$, which can be approximated by the electron diamagnetic velocity [35] (as it has been done in section 3.1) for discharges lacking NBI heating as

$$-v_{i,dia} \approx v_{e,dia} = \frac{\nabla p_e}{e n_e B_t}. \quad (9)$$

This is verified in figure 11(*a*), where $v_{e,dia} \approx v_{E\times B}$ within the errorbars (blue pluses and red triangles). It should be noted that this agreement is only valid at the radial position of the QCM, but not further inside. For discharge #39605, the plasma $E \times B$ velocity is between -10 km s^{-1} and -5 km s^{-1} during the whole discharge. The negative sign implies that the plasma rotates in electron diamagnetic direction. In addition to the $E \times B$ background velocity, the velocity of the QCM in the laboratory frame is marked as black dots in figure 11(*a*) and is approximately constant over time at a value of $v_{lab} \approx -3.5\text{ km s}^{-1}$.

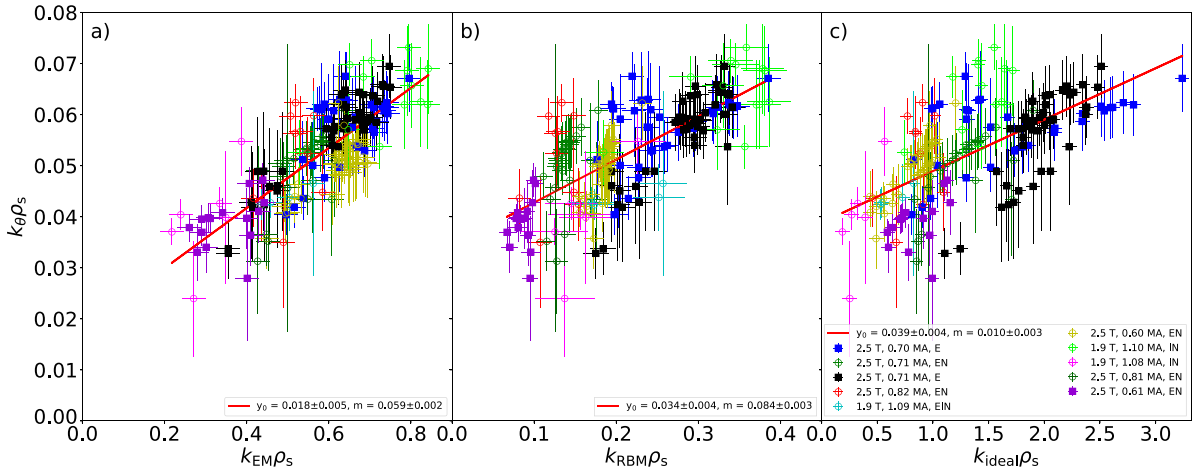

Figure 9. For numerous discharges the normalized poloidal wavenumber is compared to characteristic wavenumbers like the electromagnetic $k_{EM}\rho_s$ (*a*), the resistive ballooning mode $k_{RBM}\rho_s$ (*b*) and the ideal ballooning instability $k_{ideal}\rho_s$ (*c*). y_0 (offset) and m (slope) are the corresponding parameters for the linear fits. The legend includes the toroidal field strength B_t, plasma current I_P and the used heating mechanism, where E: ECRH, I: ICRH, N: NBI.

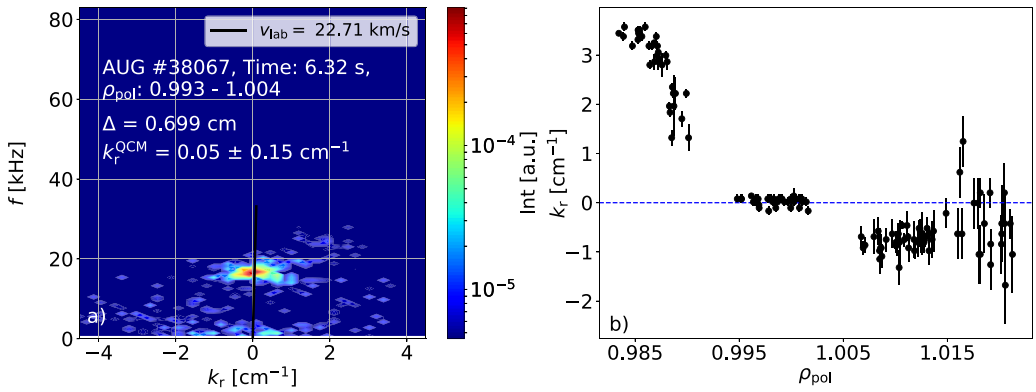

Figure 10. Example of a $k_r - f$ spectrum from discharge #38067 (*a*), where the bright point marks the QCM. The radial profile of the radial wavenumber k_r is shown in (*b*) and is approximately zero for a wide radial range.

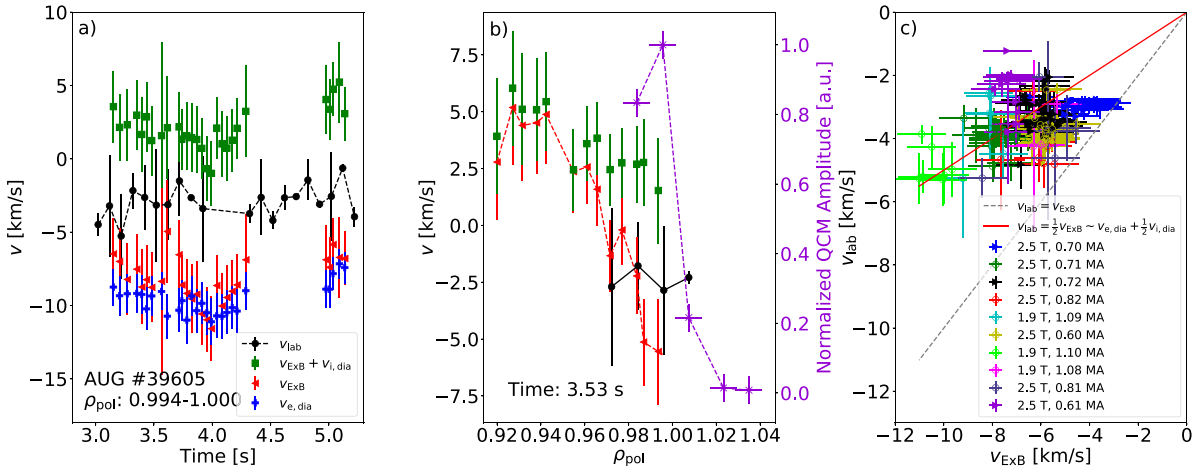

Figure 11. Comparison of $v_{E\times B}$ from CXRS, the approximated plasma velocity $v_{e,dia}$ and v_{lab}, obtained from the $k_\theta - f$ spectra (*a*) in discharge #39605. One radial profile of the velocities is shown together with the amplitudes of the Fourier spectra along the radial axis (purple crosses) as described in section 3.1 in (*b*). (*c*) shows an overview of all discharges analysed with the approximation $v_{e,dia} \approx v_{E\times B}$. The legend includes the toroidal field strength B_t and plasma current I_P.

The green squares are the sum of the ion diamagnetic velocity $v_{\mathrm{i,dia}}$ and $v_{\mathrm{E\times B}}$, obtained by CXRS. Here, a value slightly above zero is achieved. The phase velocity of the QCM in the plasma frame is calculated by the difference of v_{lab} and $v_{\mathrm{E\times B}}$. Remarkably, v_{lab} (black dots) is constantly above the background velocity, indicating that $v_{\mathrm{pl}} = v_{\mathrm{lab}} - v_{\mathrm{E\times B}} > 0\ \mathrm{km\,s^{-1}}$, so that the QCM phase velocity is in ion diamagnetic direction in the plasma frame at the position, at which the QCM is located. Though, the phase velocity in the plasma frame is smaller than the ion diamagnetic velocity, $v_{\mathrm{i,dia}}$ (black dots below green squares), which was determined according to equation (9) but with ion data instead of electron data.

Figure 11(*b*) present radial profiles of the different velocities. f_{QCM} as well as k_θ do not change drastically along the radial positions, leading to a nearly constant v_{lab} over a certain radial range. On the contrary, $v_{\mathrm{E\times B}}$ varies radially, where its highest absolute value is reached inside the E_{r} well. Combining $v_{\mathrm{E\times B}}$ and v_{lab}, it seems that the direction of motion of the QCM in the plasma frame changes with ρ_{pol}, i.e. the determination of v_{pl} seems to depend on the considered radial position, illustrated in figure 11(*b*). This fact might explain the contradicting results from Theiler *et al* [22], claiming that the QCM moves in ion diamagnetic direction and localized near the E_{r} minimum, and LaBombard *et al* [23], observing the QCM in Ohmic EDA H-modes in the near SOL with a movement in electron diamagnetic direction. In order to obtain a unique value of the plasma velocity for the QCM in our case, we assume that the relevant radial position of the QCM is located where the maximum mode amplitude is found, as described in section 3.1. We determine v_{lab} and $v_{\mathrm{E\times B}}$ at this location, e.g. at $\rho_{\mathrm{pol}} = 0.995$ in figure 11(*b*) to calculate v_{pl}.

By using the approximation $|v_{\mathrm{i,dia}}| \approx v_{\mathrm{e,dia}} \approx v_{\mathrm{E\times B}}$, it is possible to compare v_{lab} with $v_{\mathrm{E\times B}}$ for all discharges analysed in figure 11(*c*), including plasmas, for which no CXRS measurements was available. As shown in figure 11(*c*), all data points are above the $E \times B$ velocity (grey dotted line), i.e. for all cases the phase velocity in the plasma frame is in the ion diamagnetic direction. The data points are symmetrically scattered around the line indicating $v_{\mathrm{pl}} \approx 1/2\ v_{\mathrm{i,dia}}$ (red). Therefore, the data is consistent with the predictions for ballooning modes where finite Larmor radius effects are taken into account [49].

3.5. EDA H-mode and QCE in an $\alpha_{\mathrm{d}} - \alpha_{\mathrm{MHD}}-$diagram

A concept of a phase space for tokamak edge turbulence was introduced first by Rogers, Drake and Zeiler (RDZ) [46] in 1998 and serves to categorize operational points of the plasma based on simulations. The underlying physics addresses the existence of some regime boundaries observed in tokamaks, namely a density limit, changes in confinement and the ideal ballooning limit. In 2021, Eich and Manz compared the theory of RDZ to separatrix values of AUG [50] using the originally proposed normalized variables α_{MHD} and α_{d}. With a number of modifications this work then led to the concept of the separatrix operational space, which is characterized by a turbulence parameter $\alpha_{\mathrm{t}} \propto q^2 n_{\mathrm{e}} Z_{\mathrm{eff}}/T_{\mathrm{e}}^2$ [50] and three typical wavenumbers k_{EM}, k_{RBM} and k_{ideal}, introduced in section 3.3. Myra *et al* associated the EDA H-mode with a characteristic regime in an $\alpha_{\mathrm{d}} - \alpha_{\mathrm{MHD}}-$diagram [51] at the separatrix, based on the theory of RDZ. We compare this theory with the experimental data at AUG, using the dimensionless MHD ballooning parameter

$$\alpha_{\mathrm{MHD}} = q^2 R\beta/\lambda_{\mathrm{p_e}} = c_{\mathrm{MHD}} \frac{q^2 n_{\mathrm{e}} s T_{\mathrm{e,sep}}}{B_{\mathrm{t}}^2 \lambda_{\mathrm{p_e}}}, \tag{10}$$

and the diamagnetic parameter

$$\alpha_{\mathrm{d}} = \frac{1}{2\pi qR}\sqrt{\frac{m_{\mathrm{i}} c_{\mathrm{s}} R}{0.51 m_{\mathrm{e}} \nu_{\mathrm{ei}}}}\frac{R^{1/4}}{\lambda_{\mathrm{p_e}}^{1/4}} = c_{\mathrm{d}} \frac{T_{\mathrm{e,sep}}}{q\lambda_{\mathrm{p_e}}^{1/4}\sqrt{n_{\mathrm{e,sep}}}}. \tag{11}$$

The local values of $n_{\mathrm{e,sep}}$ and $T_{\mathrm{e,sep}}$ are taken at 1 mm inside the separatrix from the Thomson scattering diagnostic [52] and $c_{\mathrm{MHD}} \approx 332 \times 10^{-22}\ \mathrm{eV^{-1}\,m^4\,T^2}$ and $c_{\mathrm{d}} \approx 128 \times 10^6\ \mathrm{eV^{-1}\,m^{-5/4}}$ are constants for ASDEX Upgrade.

These two parameters control the transport in the edge of the tokamak. In general, a region for large $\alpha_{\mathrm{MHD}} > \alpha_{\mathrm{c}}$ indicates the ideal MHD limit, at which the plasma gets unstable to ideal ballooning modes (IB). For our discharges analysed it holds that $\alpha_{\mathrm{c}} > 2.51$. On the other hand, if $\alpha_{\mathrm{MHD}} < \alpha_{\mathrm{c}}$ and $\alpha_{\mathrm{d}} < 1$, the stability conditions in the plasma edge give rise to a resistive ballooning mode (RB). This condition is typically fulfilled in AUG H-mode operation [50]. By including X-Point physics, it is possible to derive regimes for IB stable plasmas and values of $\alpha_{\mathrm{d}} > 1$, that are unstable to resistive X-point modes (RX and RX-EM). These regimes have been derived by Myra and D'ippolito in [51]. All operational points of the considered discharges are characterized as unstable to resistive X-point modes with an electromagnetic fingerprint (RX-EM) in figure 12(*a*) as also proposed in [51].

Two branches are found: one following the blue triangles (EDA H-modes) and one the red spheres (QCE). The differentiation between EDA H-mode discharges and QCE plasmas was done by means of the boundary of bandwidth according to equation (4). The different slopes of the two branches can be explained by the variety of $n_{\mathrm{e,sep}}$ and $T_{\mathrm{e,sep}}$ as shown in figure 12(*b*). EDA H-modes are characterized by smaller $n_{\mathrm{e,sep}}$ and in general by a relatively small variation of densities, explaining the larger values of α_{d} at smaller values of α_{MHD}. QCE plasmas extend over a wider range of densities and temperatures, and the way this type of discharges are operated, e.g. by applying higher plasma currents and heating power for higher fuelling rates, lead to a simultaneous increase in density and temperature at the separatrix. Consequently, the α_{MHD} parameter rises faster relative to α_{d} resulting in a steeper slope of the QCE data points in figure 12(*a*). It has to be mentioned that only a subset of data points are presented here and a general overview, containing more data is work in progress. The fact that the QCE discharges (characterized by $\Delta f_{\mathrm{QCM}} > 10kHz$) appear at higher densities as shown in figure 12(*b*) implies that the coherence of the QCM decreases with density.

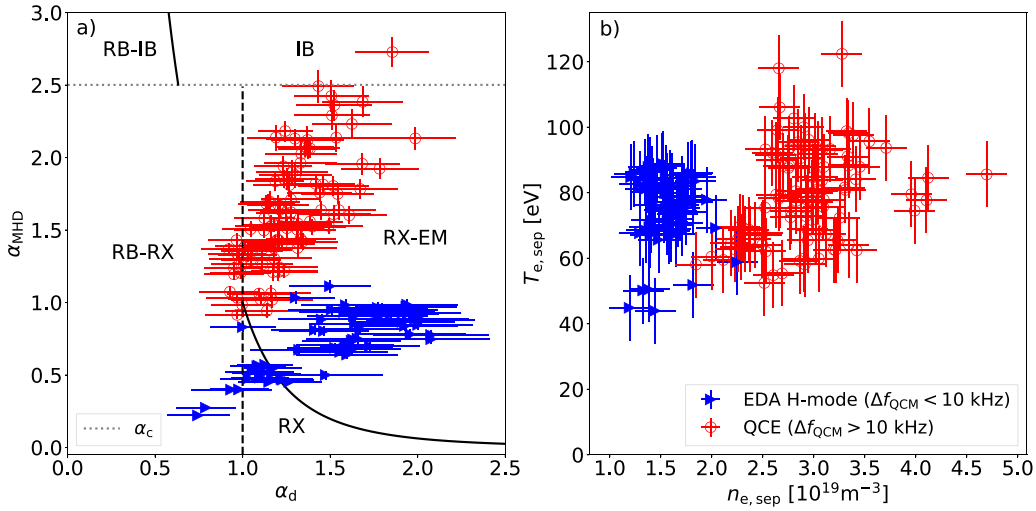

Figure 12. Classification of various discharges into an edge phase space turbulence diagram in terms of α_{MHD} and α_d, where $\alpha_{MHD} > \alpha_c \approx 2.51$ implies that the plasma is ideal ballooning (IB) unstable, $\alpha_d < 1$ indicates a resistive ballooning (RB) unstable regime and $\alpha_d > 1$ lead to resistive X-point modes (RX and RX-EM) (*a*). Blue triangles are identified as EDA H-modes, whereas red hollow circles are QCE discharges. The two regimes are also well separated in the separatrix $n_{e,sep} - T_{e,sep}$ graphic (*b*).

4. Discussion

After presenting the properties of the QCM, we discuss and classify the obtained results and compare those with preceding and ongoing analyses.

For the physical interpretation of the measurements we introduced necessary assumptions. First, the most crucial point is the radial localization of the QCM. We decided to define the QCM position at the radial location, where density and temperature fluctuation peaks. This corresponds to the maximum amplitude of the line ratio time trace along the radius. In order to support this approach, we have already shown in [29] and also in appendix B that the ratio of two emission intensities shows a maximum, where the highest density or temperature fluctuation is present. Second, the background velocity $v_{E\times B}$ was approximated by the diamagnetic velocity of the electrons and small deviations are possible. Where available this was compared to the more precise CXRS data, justifying the approximation. Third, all profile data are subject to inaccuracies inherent to the equilibrium reconstruction, which was needed to map the radial profiles of the different diagnostic onto each other. Only on the basis of these assumptions and the involved inaccuracies the following statements hold.

The QCM propagates in ion diamagnetic direction (IDD) in the plasma frame for each discharge (section 3.4), explaining the counter-intuitive relation between f_{QCM} and $v_{E\times B}$, i.e. the QCM propagates against the direction of the background plasma (section 3.1). This conclusion relies on the precision of the radial localization of the mode and the accuracy of the radial profiles, since already a small radial shift by 3 mm would lead to a propagation in electron diamagnetic direction (EDD) (cf figure 11(*b*)). Based on the measured velocity, which is determined to be in IDD by means of our approach, a whole group of modes, i.e. modes which are typically propagating in EDD, can be excluded. Qualitatively, IDD propagation applies to ideal (IBM), resistive (RBM), kinetic ballooning modes (KBM) or ion temperature gradient modes (ITG), which remain as candidates for the QCM. Furthermore, IBMs and RBMs propagate with $v_{pl}^{(I-R)BM} \geqslant 1/2 v_{i,dia}$ [49], which is in agreement with the experimentally observed results from figure 11(*c*).

All remaining candidate instabilities, i.e. IBMs [53], RBMs [54], KBMs [55] and ITGs [56] possess typical perpendicular wavenumbers lying within the range of the experimentally measured, normalized poloidal wavenumbers $0.025 < k_\theta \rho_s < 0.075$. However, the absolute values of the experimental $k_\theta \rho_s$ are significantly lower than the ones delivered theoretically by the DALF system (see figure 9). For the electromagnetic wavenumber, i.e. $k_\theta \rho_s \ll k_{EM} \rho_s$ it means that the performed discharges are deep in the electromagnetic regime and for $k_{EM} \rho_s \gtrsim 0.5$ the QCM gives rise to very strong electromagnetic turbulent transport [47], which is in agreement with the properties of KBMs. The postulated electromagnetic nature inferred from the wavenumber measurement matches the observation of the QCM in the magnetic signal (e.g. in figure 5). Generally, ITG turbulence is strongly reduced in the electromagnetic regime [57, 58], so that ITGs can be ruled out as a candidate.

The separatrix analysis (section 3.5) indicates that EDA H-modes and QCE discharges are neither unstable regarding IBMs ($\alpha_{MHD} < \alpha_c$) nor RBMs ($\alpha_d > 1$). However, IBMs and RBMs still can exist in H-modes, i.e. the regimes shown in figure 12(*a*) are not exclusive for their existence. According to the $\alpha_d - \alpha_{MHD}$−diagram at the separatrix, EDA H-modes and QCE discharges should give rise to an X-point mode with electromagnetic fingerprint (RX-EM), which cannot be generally confirmed yet disproved in experiments so far, but this result is in agreement with the simulations in [51, 59].

Simulations with the JOREK code [60] of an EDA H-mode can reproduce resistive peeling-ballooning modes with $n = 6$ to $n = 9$, resembling higher harmonic modes, similar to those being visible in the magnetic coils. Though, the poloidal

wavenumber and frequency in the simulation is close to the one of the QCM, but no harmonics of the QCM are visible in the experiment. As shown in section 3.2 the QCM is not a result of the HHMs or vice versa. Additionally, the HHMs are not well visible in QCE discharges (either the HHMs do not exist there, or we do not detect those), but QCE scenarios also do not exhibit major type-I ELMs generally, so that the HHMs do not seem to be the relevant characteristic for ELM avoidance.

Harrer *et al* [15] showed that a common feature of QCE discharges is that they are very close to the ideal $n \to \infty$ ballooning stability limit at $\rho_{\mathrm{pol}} = 0.99$, i.e. inside the separatrix. This unstable region is overlapping with the radial range at which the QCM has its highest amplitude in our experiments. Figure 12(*a*) shows that QCE discharges are closer to the ideal MHD stability limit at the separatrix than EDA H-modes. Initial investigations of the ideal ballooning stability threshold in EDA H-mode discharges indicate that the pedestal is ballooning unstable over a wider region. However, a comprehensive study is work in progress.

The characterization of the QCM and the measured QCM properties presented here leave three instability candidates for the QCM: IBM, RBM or KBM.

A potential quantitative comparison of the found experimental results with MHD codes like CASTOR3D [61] and gyro kinetic codes like GENE [56] are envisaged.

Moreover, for the purpose of this paper a differentiation between EDA H- and QCE discharges has been achieved explicitly by solely considering the QCM frequency bandwidth as the distinguishing parameter. In addition, the existence or visibility of the HHMs in the magnetic coils support the differentiation of the two regimes. The arbitrary boundary of equation (4) shows good agreement with the behaviours of the two scenarios in the $\alpha_{\mathrm{d}} - \alpha_{\mathrm{MHD}}$−diagram from figure 12(*a*) and should give an impulse for future work regarding the separation of these regimes.

5. Conclusion

This paper provided a comprehensive characterization of the quasi-coherent mode, appearing in EDA H-modes and QCE plasmas, using the THB diagnostic at ASDEX Upgrade with the following observations. We observed that the quasi-coherent mode appears in both EDA H-modes and QCE plasmas and proposed that the quasi-coherent mode can be used to distinguish the regimes. The separation criterion: $\Delta f_{\mathrm{QCM}} = 10$ kHz has been used for this purpose. This criterion also separated EDA H-modes and QCE discharges reasonably by two different branches in a separatrix $\alpha_{\mathrm{d}} - \alpha_{\mathrm{MHD}}$−diagram for the limited subset analysed. Qualitatively, EDA H-modes have a smaller value of α_{MHD} than QCE discharges, but all data points are below the critical ideal MHD limit, i.e. $\alpha_{\mathrm{MHD}} < \alpha_{\mathrm{c}}$, and the diamagnetic parameter is always $\alpha_{\mathrm{d}} > 1$. EDA H-modes are accompanied with higher harmonic modes, which are exclusively visible in magnetic pick-up coils. However, the quasi-coherent mode is an independent mode driven by a separate mechanism, which coexists and couples with the higher harmonic modes.

The quasi-coherent mode is localized close to the separatrix and the E_{r} minimum at around $\rho_{\mathrm{pol}}^{\mathrm{QCM}} = 0.993 \pm 0.007$ and its frequency shows a dependence on the poloidal plasma beta, i.e. $f_{\mathrm{QCM}} R_0 / c_{\mathrm{s}} \propto 1/\beta_{\mathrm{pol}}^2$. The normalized poloidal wavenumber is in a range of $0.025 < k_\theta \rho_{\mathrm{s}} < 0.075$ and scales with the electromagnetic wavenumber $k_{\mathrm{EM}} \rho_{\mathrm{s}} \propto \sqrt{\beta}$, whereas the radial wavenumber vanishes, suggesting a streamer-like appearance. We showed that the quasi-coherent mode is visible in magnetic pick-up coils, emphasizing the electromagnetic character of it. The mode has a phase velocity in the plasma frame in the ion diamagnetic direction of approximately $v_{\mathrm{pl}} \approx 1/2\, v_{\mathrm{i,dia}}$.

All observations are consistent with electromagnetic ballooning modes, like ideal, resistive or kinetic ballooning modes.

Acknowledgments

This work has been carried out within the framework of the EUROfusion Consortium, funded by the European Union via the Euratom Research and Training Programme (Grant Agreement No 101052200—EUROfusion). Views and opinions expressed are however those of the author(s) only and do not necessarily reflect those of the European Union or the European Commission. Neither the European Union nor the European Commission can be held responsible for them. J Kalis, D Wendler and G Birkenmeier received funding from the Helmholtz Association under Grant No. VH-NG-1350.

Appendix A. Discharges

In table A1 all single discharges analysed are displayed with various quantities like toroidal magnetic field strength B_{t}, plasma current I_{P}, edge safety factor q_{95} and heating powers P for Electron and Ion Cyclotron Heating (ECRH, ICRH) and Neutral Beam Injection (NBI). Additionally, the type of the corresponding discharge (EDA H-mode or QCE, according to equation (4)), the number of QCM data points acquired from each shot and the radial position of the QCM, $\rho_{\mathrm{pol}}^{\mathrm{QCM}}$, is shown. The discharge #40110 is shown in figure 4 as a transition discharge, starting in EDA H-mode and ending in QCE.

Appendix B. Simulations of the radial localization via the THB

A synthetic diagnostic has been set up in [29] to understand different diagnostic effects of thermal Helium beam (THB) or gas-puff imaging (GPI) diagnostics in general regarding the interpretation of the generated data. The total line emission intensity by one individual spectral line is given by

$$I_\lambda = n_{\mathrm{He}} n_{\mathrm{e}} \mathrm{PEC}_\lambda \left(n_{\mathrm{e}}, T_{\mathrm{e}}\right), \tag{B.1}$$

where n_{He} is the neutral Helium density and $\mathrm{PEC}_\lambda \left(n_{\mathrm{e}}, T_{\mathrm{e}}\right)$ is the corresponding photo emission coefficient for each

Table A1. Discharges and corresponding parameters.

Discharge	Type	#data points	5×5 Grid	B_t (T)	I_P (MA)	q_{95}	P_{ECRH} (MW)	P_{ICRH} (MW)	P_{NBI} (MW)	ρ_{pol}^{QCM}
#36124	EDA	52	No	2.50	0.79	5.30	3.0	0.0	0.0	0.998(007)
#38067	EDA	37	Yes	2.50	0.70	5.61	3.5	0.0	0.0	0.990(006)
#39400	QCE	22	Yes	2.50	0.71	5.66	3.5	0.0	2.5	0.995(007)
#39404	EDA	15	Yes	2.50	0.71	5.61	2.4	0.0	Blip	0.989(009)
#39541	QCE	16	Yes	2.45	0.82	4.87	2.4	0.0	2.5	0.995(008)
#39605	QCE	16	Yes	1.90	1.09	3.20	0.2	3.7	5.0	0.995(009)
#39666	EDA	23	Yes	2.50	0.60	6.48	1.4	0.0	2.5	0.988(006)
#40110	EDA/QCE	28	No	2.51	0.71	5.61	3.5	3.7	Blip	0.992(010)
#40226	QCE	17	Yes	1.90	1.10	3.21	0.0	3.8	4.1	0.995(006)
#40227	QCE	7	Yes	1.90	1.08	3.21	0.0	3.9	4.1	0.994(007)
#40613	QCE	11	Yes	2.50	0.81	5.49	4.4	0.0	5.0	0.995(006)
#40637	QCE	35	No	2.50	0.80	5.52	4.4	0.0	5.0	0.993(008)
#40647	EDA	65	Yes	2.52	0.60	6.63	1.9	0.0	0.0	0.989(007)

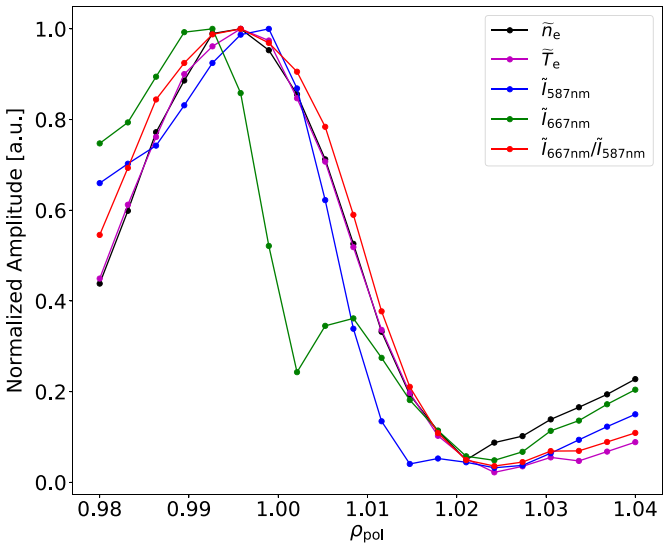

Figure B1. A Gaussian-like synthetic density $\widetilde{n}_e$ and temperature $\widetilde{T}_e$ fluctuation is displayed correctly by the ratio of the line intensities I_2/I_1, but not by the individual ones. The amplitudes in the Fourier spectra have been normalized to their corresponding maximum.

wavelength λ, depending on n_e and T_e. The PEC_λ is different for each spectral line, but for the analysis in the paper only $\lambda_2 = 667$ nm and $\lambda_1 = 587$ nm are used.

We implemented a Gaussian-like density $\widetilde{n}_e$ and temperature fluctuation $\widetilde{T}_e$, representing the impact of the QCM, with maximum fluctuation at $\rho_{pol} = 0.995$ and a radial width of $\Delta\rho_{pol} = 0.01$. The mode is localized, where the highest normalized amplitude in the Fourier spectra can be found. Therefore, we divided the peak value by the average intensity in the Fourier spectra. It is visible in figure B1 that both, the line emission intensity for λ_1, i.e. $\widetilde{I}_{587nm}$ and λ_2, i.e. $\widetilde{I}_{667nm}$ lead to a wrong localization of the fluctuation. On the other hand, their ratio delivers the correct localization, i.e. the position where the pre-implemented $\widetilde{n}_e$ and $\widetilde{T}_e$ are the largest. Thus, the highest amplitude of the measured signal $\widetilde{I}_{667nm}/\widetilde{I}_{587nm}$ in the Fourier spectrum is equal to the position of the maximum impact of the mode.

Appendix C. Arrangement of the LOS of the THB

At ASDEX Upgrade it is possible to change the channel arrangement of the THB between a highly radial resolved grid (radial), shown in figure C1(*a*) and a 5×5 grid, with which poloidal and radial analyses are possible, depicted in figure C1(*b*). Whereas the radial arrangement is mainly used to analyse the radial localization, the 5×5 grid enables the possibility to determine poloidal quantities like the poloidal wavenumber k_θ, for which the distance between two poloidally arranged LOS, Δ, is necessary. Furthermore, the magnetic geometry and thus, the position of the separatrix can be varied.

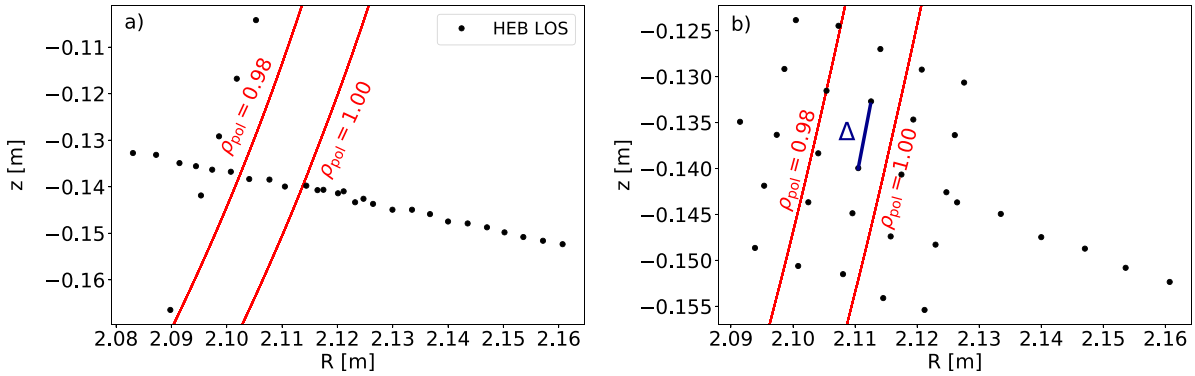

Figure C1. Two THB grid possibilities: either the line of sights are distributed solely radially (*a*) or in a 5 × 5 grid, enabling poloidal and radial analyses (*b*). Δ is the distance between two poloidal LOS.

ORCID iDs

J. Kalis https://orcid.org/0000-0001-8170-1375
G. Birkenmeier https://orcid.org/0000-0001-7508-3646
P. Manz https://orcid.org/0000-0002-5724-0174
T. Eich https://orcid.org/0000-0003-3065-8420
M. Griener https://orcid.org/0000-0003-2953-536X
L. Gil https://orcid.org/0000-0002-9970-2154
M. Faitsch https://orcid.org/0000-0002-9809-7490
D. Wendler https://orcid.org/0000-0002-8838-0137
U. Stroth https://orcid.org/0000-0003-1104-2233

References

[1] Wagner F. 2007 *Plasma Phys. Control. Fusion* **49** B1
[2] Zohm H. 1996 *Plasma Phys. Control. Fusion* **38** 105
[3] Shimada M. *et al* 2007 *Nucl. Fusion* **47** 01
[4] Evans T. *et al* 2005 *Nucl. Fusion* **45** 595
[5] Viezzer E. *et al* 2022 *Nucl. Mater. Energy* **34** 101308
[6] Greenwald M. *et al* 1999 *Phys. Plasmas* **6** 1943
[7] Paz-Soldan C. (The DIII-D Team) 2021 *Plasma Phys. Control. Fusion* **63** 083001
[8] Mossessian D., Groebner R.J., Moyer R.A., Osborne T.H., Hughes J.W., Greenwald M., Hubbard A. and Rhodes T.L. 2003 *Phys. Plasmas* **10** 689–98
[9] Sun P. *et al* 2019 *Phys. Plasmas* **26** 012304
[10] Gil L. *et al* 2020 *Nucl. Fusion* **60** 054003
[11] Kirk A., Muller H.W., Wolfrum E., Meyer H., Herrmann A., Lunt T., Rohde V. and Tamain P. 2011 *Plasma Phys. Control. Fusion* **53** 095008
[12] Labit B. *et al* 2019 *Nucl. Fusion* **59** 086020
[13] Saibene G. *et al* 2005 *Nucl. Fusion* **45** 297
[14] Faitsch M., Eich T., Harrer G.F., Wolfrum E., Brida D., David P., Griener M. and Stroth U. 2021 *Nucl. Mater. Energy* **26** 100890
[15] Harrer G.F. *et al* 2022 *Phys. Rev. Lett.* **129** 165001
[16] Griener M. *et al* 2020 *Nucl. Mater. Energy* **25** 100854
[17] Sips A. *et al* 2018 *Nucl. Fusion* **58** 126010
[18] Faitsch M., Eich T., Harrer G.F., Wolfrum E., Brida D., David P., Dunne M., Gil L., Labit B. and Stroth U. 2023 *Nucl. Fusion* **63** 076013
[19] Griener M. *et al* 2018 *Plasma Phys. Control. Fusion* **60** 025008
[20] Vanovac B. *et al* 2023 *EPJ Web Conf.* **277** 03003
[21] Wolfrum E. *et al* 2011 *Plasma Phys. Control. Fusion* **53** 085026
[22] Theiler C., Terry J.L., Edlund E., Cziegler I., Churchill R.M., Hughes J.W., LaBombard B. and Golfinopoulos T. 2017 *Plasma Phys. Control. Fusion* **59** 025016
[23] Labombard B., Golfinopoulos T., Terry J.L., Brunner D., Davis E., Greenwald M. and Hughes J.W. 2014 *Phys. Plasmas* **21** 056108
[24] Siccinio M. *et al* 2020 *Fusion Eng. Des.* **156** 111603
[25] Griener M., Wolfrum E., Cavedon M., Dux R., Rohde V., Sochor M., Muñoz Burgos J.M., Schmitz O. and Stroth U. 2018 *Rev. Sci. Instrum.* **89** 10D102
[26] Strait E., Fredrickson E.D., Moret J.-M. and Takechi M. 2008 *Fusion Sci. Technol.* **53** 304
[27] Wendler D., Dux R., Fischer R., Griener M., Wolfrum E., Birkenmeier G. and Stroth U. 2022 *Plasma Phys. Control. Fusion* **64** 045004
[28] Stotler D.P., Labombard B., Terry J. and Zweben S. 2003 *J. Nucl. Mater.* **313–316** 1066
[29] Griener M., Kalis J., Wendler D., Birkenmeier G., Wolfrum E., McDermott R.M. and Stroth U. 2022 *Nucl. Mater. Energy* **34** 101346
[30] De La Cal E. and Guasp J. 2011 *Plasma Phys. Control. Fusion* **53** 085006
[31] De La Cal E. 2015 *Plasma Phys. Control. Fusion* **57** 075001
[32] Kallenbach A. *et al* 2020 *Nucl. Fusion* **61** 016002
[33] Fischer R., Fuchs C.J., Kurzan B., Suttrop W. and Wolfrum E. 2010 *Fusion Sci. Technol.* **58** 675
[34] Donoghue T. *et al* 2020 *Nat. Neurosci.* **23** 1655
[35] Viezzer E., Pütterich T., Angioni C., Bergmann A., Dux R., Fable E., McDermott R.M., Stroth U. and Wolfrum E. 2014 *Nucl. Fusion* **54** 012003
[36] CAVEDON M., Pütterich T., Viezzer E., Dux R., Geiger B., McDermott R.M., Meyer H. and Stroth U. 2017 *Rev. Sci. Instrum.* **88** 43103
[37] Solano E.R. *et al* 2017 *Nucl. Fusion* **57** 022021
[38] Birkenmeier G. *et al* 2016 *Nucl. Fusion* **56** 086009
[39] Grover O. *et al* 2023 *Nucl. Fusion* accepted (https://doi.org/10.1088/1741-4326/ad0eae)
[40] Manz P. *et al* 2016 *Phys. Plasmas* **23** 052302
[41] Snipes J., LaBombard B., Greenwald M., Hutchinson I.H., Irby J., Lin Y., Mazurenko A. and Porkolab M. 2001 *Plasma Phys. Control. Fusion* **43** L23
[42] Mink F., Wolfrum E., Maraschek M., Zohm H., Horváth L., Laggner F.M., Manz P., Viezzer E. and Stroth U. 2016 *Plasma Phys. Control. Fusion* **58** 125013
[43] Ritz C. *et al* 1988 *Rev. Sci. Instrum.* **59** 1739
[44] Beall J.M., Kim Y.C. and Powers E.J. 1982 *J. Appl. Phys.* **53** 3933
[45] Scott B.D. 2005 *New J. Phys.* **7** 92
[46] Rogers B.N., Drake J.F. and Zeiler A. 1998 *Phys. Rev. Lett.* **81** 4396

[47] Eich T. and Manz P. (the ASDEX Upgrade team) 2021 *Nucl. Fusion* **61** 086017
[48] Cheng J. *et al* 2020 *Nucl. Fusion* **60** 046021
[49] Aiba N. 2016 *Plasma Phys. Control. Fusion* **58** 045020
[50] Eich T., Manz P., Goldston R.J., Hennequin P., David P., Faitsch M., Kurzan B., Sieglin B. and Wolfrum E. 2020 *Nucl. Fusion* **60** 056016
[51] Myra J. and D'ippolito D. 2005 *Phys. Plasmas* **12** 092511
[52] Kurzan B. and Murmann H.D. 2011 *Rev. Sci. Instrum.* **82** 101101
[53] Halpern F.D., Jolliet S., Loizu J., Mosetto A. and Ricci P. 2013 *Phys. Plasmas* **20** 052306
[54] Bourdelle C., Garbet X., Singh R. and Schmitz L. 2012 *Plasma Phys. Control. Fusion* **54** 115003
[55] Yan Z., McKee G.R., Groebner R.J., Snyder P.B., Osborne T.H., Beurskens M.N. and Burrell K.H. 2011 *Phys. Plasmas* **18** 056117
[56] Told D., Jenko F., Xanthopoulos P., Horton L.D. and Wolfrum E. 2008 *Phys. Plasmas* **15** 102306
[57] Whelan G.G., Pueschel M. and Terry P. 2018 *Phys. Rev. Lett.* **120** 175002
[58] Pueschel M. and Jenko F. 2010 *Phys. Plasmas* **17** 062307
[59] Mazurenko A., Porkolab M., Mossessian D., Snipes J.A., Xu X.Q. and Nevins W.M. 2001 *Phys. Rev. Lett.* **89** 225004
[60] Cathey A. *et al* 2023 *Nucl. Fusion* **63** 062001
[61] Strumberger E. and Günter S. 2017 *Nucl. Fusion* **57** 016032